Earth and Planetary Science Letters 450 (2016) 263–273

Contents lists available at ScienceDirect

Earth and Planetary Science Letters

www.elsevier.com/locate/epsl

Noble gas composition of subcontinental lithospheric mantle: An extensively degassed reservoir beneath Southern Patagonia

Tiago Jalowitzki [a,b,*], Hirochika Sumino [b,2], Rommulo V. Conceição [a], Yuji Orihashi [c], Keisuke Nagao [b,1], Gustavo W. Bertotto [d], Eduardo Balbinot [e], Manuel E. Schilling [f], Fernanda Gervasoni [g]

[a] Programa de Pós–graduação em Geociências, Universidade Federal do Rio Grande do Sul (UFRGS). Av. Bento Gonçalves, 9500 – Prédio 43129, Porto Alegre – RS, Brazil
[b] Geochemical Research Center, Graduate School of Science, University of Tokyo, 7-3-1 Hongo, Bunkyo-ku, Tokyo 113-0033, Japan
[c] Earthquake Research Institute, University of Tokyo, 1-1-1 Yayoi, Bunkyo-ku, Tokyo 113-0032, Japan
[d] CONICET – Universidad Nacional de La Pampa, Uruguay 151 (6300), Santa Rosa, La Pampa, Argentina
[e] Department of Physics, University of Surrey, Guildford GU2 7XH, UK
[f] Instituto de Ciencias de la Tierra, Facultad de Ciencias, Universidad Austral de Chile, Valdivia, Código postal 5090000, Región de Los Ríos, Chile
[g] Institut für Mineralogie, Westfählische–Wilhelms-Universität Münster, Germany

ARTICLE INFO

Article history:
Received 1 December 2015
Received in revised form 17 June 2016
Accepted 21 June 2016
Available online xxxx
Editor: B. Marty

Keywords:
noble gas isotopes
subcontinental lithospheric mantle
radiogenic isotopes
mantle xenoliths
Southern Patagonia

ABSTRACT

Patagonia, in the Southern Andes, is one of the few locations where interactions between the oceanic and continental lithosphere can be studied due to subduction of an active spreading ridge beneath the continent. In order to characterize the noble gas composition of Patagonian subcontinental lithospheric mantle (SCLM), we present the first noble gas data alongside new lithophile (Sr–Nd–Pb) isotopic data for mantle xenoliths from Pali-Aike Volcanic Field and Gobernador Gregores, Southern Patagonia. Based on noble gas isotopic compositions, Pali-Aike mantle xenoliths represent intrinsic SCLM with higher $(U+Th+K)/(^{3}He, ^{22}Ne, ^{36}Ar)$ ratios than the mid-ocean ridge basalt (MORB) source. This reservoir shows slightly radiogenic helium ($^{3}He/^{4}He = 6.84–6.90\ R_A$), coupled with a strongly nucleogenic neon signature (mantle source $^{21}Ne/^{22}Ne = 0.085–0.094$). The $^{40}Ar/^{36}Ar$ ratios vary from a near-atmospheric ratio of 510 up to 17700, with mantle source $^{40}Ar/^{36}Ar$ between 31100^{+9400}_{-6800} and 54000^{+14200}_{-9600}. In addition, the $^{3}He/^{22}Ne$ ratios for the local SCLM endmember, at 12.03 ± 0.15 to 13.66 ± 0.37, are higher than depleted MORBs, at $^{3}He/^{22}Ne = 8.31–9.75$. Although asthenospheric mantle upwelling through the Patagonian slab window would result in a MORB-like metasomatism after collision of the South Chile Ridge with the Chile trench ca. 14 Ma, this mantle reservoir could have remained unhomogenized after rapid passage and northward migration of the Chile Triple Junction. The mantle endmember xenon isotopic ratios of Pali-Aike mantle xenoliths, which is first defined for any SCLM-derived samples, show values indistinguishable from the MORB source ($^{129}Xe/^{132}Xe = 1.0833^{+0.0216}_{-0.0053}$ and $^{136}Xe/^{132}Xe = 0.3761^{+0.0246}_{-0.0034}$).
The noble gas component observed in Gobernador Gregores mantle xenoliths is characterized by isotopic compositions in the MORB range in terms of helium ($^{3}He/^{4}He = 7.17–7.37\ R_A$), but with slightly nucleogenic neon (mantle source $^{21}Ne/^{22}Ne = 0.065–0.079$). We suggest that this MORB-like metasomatism was capable of overprinting the noble gas composition of Gobernador Gregores due to recent metasomatism of the SCLM because of asthenospheric mantle upwelling in response to opening of the Patagonian slab window. The $^{40}Ar/^{36}Ar$ ratios vary from a near-atmospheric ratio of 380 up to 6560, with mantle source $^{40}Ar/^{36}Ar$ between 8100^{+1400}_{-700} and 17700^{+4400}_{-3100}. The lower $^{40}Ar/^{36}Ar$ ratio of the

* Corresponding author at: Programa de Pós–graduação em Geociências, Instituto de Geociências, Universidade Federal do Rio Grande do Sul (UFRGS). Av. Bento Gonçalves, 9500 – Prédio 43129, Bairro Agronomia, Porto Alegre – RS, Brazil. CEP: 91501970.

E-mail addresses: tiago.jalowitzki@ufrgs.br (T. Jalowitzki), sumino@igcl.c.u-tokyo.ac.jp (H. Sumino), rommulo.conceicao@ufrgs.br (R.V. Conceição), oripachi@eri.u-tokyo.ac.jp (Y. Orihashi), nagao@kopri.re.kr (K. Nagao), gwbertotto@yahoo.com.ar (G.W. Bertotto), e.balbinot@surrey.ac.uk (E. Balbinot), manuel.schilling@uach.cl (M.E. Schilling), gervasoni.fe@uni-muenster.de (F. Gervasoni).

[1] Present address: Division of Polar Earth-System Sciences, KOPRI (Korea Polar Research Institute), 26 Songdomirae-ro, Yeonsu-gu, Incheon 21990, Korea.
[2] Present address: Department of Basic Science, Graduate School of Arts and Sciences, University of Tokyo, 3-8-1 Komaba, Meguro-ku, Tokyo 153-8902, Japan.

http://dx.doi.org/10.1016/j.epsl.2016.06.034

Gobernador Gregores mantle source, compared with that of Pali-Aike, attests that the Patagonia SCLM was affected significantly by atmospheric contamination associated with the recycled oceanic lithosphere.

1. Introduction

Ultramafic mantle xenoliths that are derived from wedges overlying subduction zones associated with ridge subduction and slab window formation are very rare. Patagonia, the southernmost portion of South America, is one of the few locations where active subduction of a spreading ridge occurs and its effects on ridge axis magmatism can be investigated. Since the middle Miocene, the Chile active spreading ridge has been subducting beneath South America, resulting in a slab-free zone, or slab window, through which asthenospheric mantle can flow. Thus, the collision of the Chile Ridge against the Chile trench offers an opportunity to investigate the composition of the subcontinental lithospheric mantle (SCLM) in this particular geological setting, which is represented by mantle xenoliths, and the influence of the shallow asthenospheric mantle beneath the Andean continental back-arc region.

Abundant spinel- and/or garnet-bearing xenoliths hosted by intraplate alkaline basalts, found in the Pali-Aike Volcanic Field (PAVF) and Gobernador Gregores (GG), provide invaluable information about the nature of southern Patagonian SCLM evolution. Subcontinental mantle xenoliths often have small quantities of noble gases trapped in fluid inclusions (e.g., Gautheron et al., 2005); however, these gases are powerful tracers of the mantle sources. Although the noble gas isotopic ratios of mid-ocean-ridge basalts (MORBs) and ocean island basalts (OIBs) are relatively well defined (e.g., Sarda et al., 1988; Moreira et al., 1998; Trieloff et al., 2000; Mukhopadhyay, 2012), the composition of the SCLM source remains poorly understood. This limitation is enhanced by the significant contribution of an air-like component to the noble gas composition of mantle-derived xenoliths. This complicates the characterization of the mantle endmember composition because these rocks generally display a binary mixture between a mantle-derived and an atmospheric component (e.g., Buikin et al., 2005; Gautheron et al., 2005; Hopp et al., 2004).

In order to determine the noble gas composition of Patagonian SCLM at the latitude of the Austral Volcanic Zone (AVZ; 49°S–55°S), we present the first helium, neon, argon, krypton, and xenon isotopic ratios plus new lithophile isotopes (Sr–Nd–Pb) in the whole-rock and in mineral separates from anhydrous and hydrous peridotites.

2. Geological setting

Geodynamically, the Patagonian continental back-arc represents a complex region formed by several continental accretion events related to the subduction of different oceanic plates (e.g., Pankhurst et al., 2006), some of which contain seismic and aseismic ridges (e.g., Chile Ridge and Juan Fernandez Ridge).

At present, the Patagonian western margin is characterized by the continuous subduction of the Nazca and Antarctic oceanic plates beneath the South American continental plate, resulting in the formation of the Andean volcanic arc. Approximately 16 Ma ago, the South Chile Ridge (SCR) collided with the Chile trench at the latitude of Tierra del Fuego (55°S) and formed a ridge–trench–trench triple junction known as the Chile Triple Junction (CTJ; Cande and Leslie, 1986). This triple point has since migrated northward to its present position north of the Taitao Peninsula (46.5°S). The subduction of four oblique active ridge segments that entered the trench at 12 Ma (SCR–2), 6 Ma (SCR–1), 3 Ma (SCR0), and 0.3 Ma (SCR1) resulted in a series of slab windows beneath the South American plate (e.g., Cande and Leslie, 1986). Subduction of these segments is associated with asthenospheric mantle upwelling and with the extensive eruption of plateau lavas from the late Miocene to the present (e.g., Gorring et al., 1997; D'Orazio et al., 2000). The ultramafic xenoliths analyzed in this study (Supplementary Table S1) were sampled from the GG volcanic center (PM23; Fig. 1) and from PAVF (PM14 and PM18; Fig. 1).

Gobernador Gregores is located ~400 km east of the Chile trench, at the southwest border of the Deseado Massif, and within the Meseta Central. The xenoliths were brought to the surface by Plio–Pleistocene alkaline basalts and hawaiites that form a post–plateau sequence (ca. 3.5 Ma; Gorring et al., 1997). The samples studied here are spinel–bearing xenoliths with anhydrous or hydrous (amphibole ± phlogopite ± apatite) assemblages that locally contain glass. These samples are similar to those reported in previous studies (e.g., Gorring and Kay, 2000; Laurora et al., 2001; Zaffarana et al., 2014).

Two different localities of PAVF (4500 km^2; D'Orazio et al., 2000) are considered in this study: 1) Laguna Ana (PM14) and 2) Laguna Timone (PM18). PAVF represents the southernmost Patagonian plateau basalts in the Andean back-arc, located ~400 km south of GG and east of the present day Chile trench (Fig. 1). PAVF is composed of more than 450 monogenetic volcanic centers composed mainly of alkaline basalts and basanites, with minor olivine basalts (e.g., D'Orazio et al., 2000). The xenoliths hosted by post–plateau alkaline basalts (3.78–0.17 Ma; e.g., D'Orazio et al., 2000 and references therein) are composed of spinel, spinel–garnet, and garnet harzburgites and lherzolites with hydrous phases such as amphibole and phlogopite (e.g., Stern et al., 1999; Gervasoni et al., 2012).

3. Analytical techniques

By using a heating method, noble gases were extracted from GG spinel peridotite samples and PAVF peridotite samples containing garnet and spinel or only spinel. Three whole-rock samples and at least one olivine sample containing the largest amounts of ^4He between 1.3×10^{-6} and 5.3×10^{-5} cm^3 STP/g, were selected from each locality to determine noble gas isotopic ratios by using the crushing method (Supplementary Tables S2–S3). Details of sample processing prior to noble gas analysis are described in the Supplementary Material. The analysis was performed at the Geochemical Research Center, Graduate School of Science, University of Tokyo. Single step heating experiments were applied to derive helium, neon, and argon isotopic ratios in the whole-rock samples (~0.5 g). All noble gas isotopic ratios (helium, neon, argon, krypton, and xenon) were obtained by stepwise crushing in a vacuum to release the noble gases trapped in fluid inclusions within the whole-rock and olivine (Supplementary Tables S2–S5). For the crushing experiments, samples >1 g were crushed in a stainless-steel tube with a sequential number of strokes from a nickel piston driven from outside the vacuum by a solenoid magnet (Sumino et al., 2001). A variable number of strokes was applied to crush the samples, such as 100, 500, 1000, and 2000; the last was applied repeatedly if the sample had sufficient quantities of noble gases. The purification, separation, and isotope ratio analysis procedures of noble gases extracted by single step heating or crushing are described in detail in the Supplementary Material. Based on the reproducibility of measurements of a Japanese helium standard (HESJ) and those

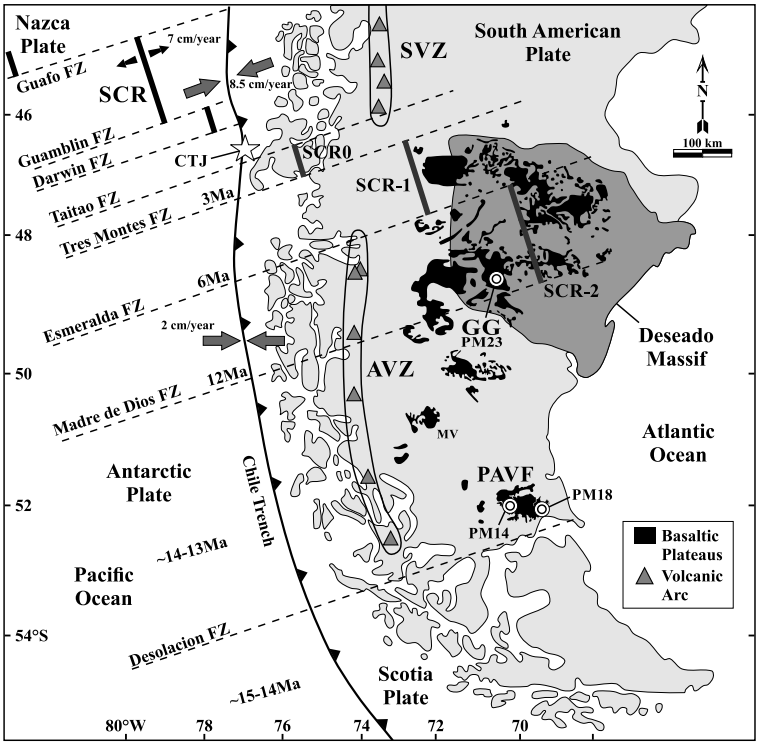

Fig. 1. Present-day tectonic setting of southern South America. Circles indicate the studied localities: Laguna Ana (PM14: 52°04′34″S; 69°47′17″W); Laguna Timone (PM18: 52°01′39″S; 70°12′53″W); Gobernador Gregores (PM23: 48°34′02″S; 70°10′59″W).

of a calibrated air standard for other noble gases, the estimated experimental uncertainties for noble gas concentrations were 5% for helium and argon, and 10% for neon, krypton and xenon. During neon analysis, corrections for $^{40}Ar^{++}$ on $^{20}Ne^{+}$ and $CO_2{}^{++}$ on $^{22}Ne^{+}$ were applied following the method described by Osawa (2004) and were determined to be <5%. Uncertainties assigned to the observed isotopic ratios were one standard deviation (1σ), including uncertainties of blank and mass discrimination corrections. Blanks were run by using the same procedure as that used for the samples. The heating blanks were: $^{4}He = (2–4) \times 10^{-11}$ cm^3 STP, $^{20}Ne = (1–9) \times 10^{-12}$ cm^3 STP, and $^{40}Ar = (2–12) \times 10^{-9}$ cm^3 STP, and the crushing blanks were: $^{4}He = (0.6–13) \times 10^{-11}$ cm^3 STP, $^{20}Ne = (2–6) \times 10^{-13}$ cm^3 STP, $^{40}Ar = (3–15) \times 10^{-10}$ cm^3 STP, $^{84}Kr = (0.4–3) \times 10^{-14}$ cm^3 STP, and $^{132}Xe = (0.5–4) \times 10^{-15}$ cm^3 STP. Assuming the higher measured blank values obtained for helium, neon, argon, krypton, and xenon, as well as eliminating the first and the last extraction steps of crushing strokes, we estimated their contributions in our data. For ^{4}He, the blank contribution was <1% for both heating and crushing experiments. Excluding the samples that showed neon isotopic ratios indistinguishable from air, the blank contribution in the heating experiments was 2–27%, whereas for crushing, the variation was 1–20% (with most <4%). For ^{40}Ar, the blank contribution was <7% for both heating and crushing experiments. For ^{84}Kr, the blank contribution in the crushing experiments was <5%. Finally, except for the samples having xenon isotopic ratios indistinguishable from air, the blank contribution in the crushing experiments was <4%. Therefore, the measured blanks confirmed negligible noble gas contributions from sources other than the sample aliquots.

The Sr–Nd–Pb isotopic ratios for seven whole-rock samples were measured at Laboratório de Geologia Isotópica, Universidade Federal do Rio Grande do Sul (UFRGS), Brazil. In addition, the Sr–Nd–Pb isotope compositions were measured on the separates of orthopyroxene, clinopyroxene, and phlogopite from the garnet-spinel harzburgite PM18–17. Details of the sample dissolution and column separation followed by Sr–Nd–Pb isotope analysis are described in the Supplementary Material. Replicate analyses of NBS–987 and JNDI standards gave $^{87}Sr/^{86}Sr = 0.710254 \pm 12$ ($n = 7$, 2σ) and $^{143}Nd/^{144}Nd = 0.512101 \pm 8$ ($n = 4$, 2σ). For Pb NBS–981 and NBS–982, variation in the accepted values was less than 0.01%/a.m.u.

4. Results

The results of noble gas isotope measurements by single step heating and stepwise crushing extraction methods for both localities (GG and PAVF) are presented in Supplementary Tables S2–S5.

4.1. Helium

The helium concentrations (^{4}He) obtained by heating experiments show a wide and variable range between 15–5300 $\times$ 10^{-8} cm^3 STP/g (PAVF) and 36–1210 $\times$ 10^{-8} cm^3 STP/g (GG). Helium isotope ratio ($^{3}He/^{4}He$; in R_A, where 1 R_A corresponds to the atmospheric ratio of 1.4×10^{-6}; Ozima and Podosek, 1983) versus total ^{4}He concentrations of each sample analyzed by crushing (Fig. 2) also show a large variability in terms of ^{4}He concentration, ranging from 36 to 1560 $\times$ 10^{-8} cm^3 STP/g (PAVF) and from 16 to 750 $\times$ 10^{-8} cm^3 STP/g (GG). No significant change is noted in the $^{3}He/^{4}He$ ratios with an increasing number of strokes during stepwise crushing (Fig. S1). The total ^{4}He concentrations found in separated olivine crystals tend to show lower values than those obtained from whole-rock samples (Fig. 2 and Supplementary Table S2).

4.2. Neon

Most neon isotopic data from both PAVF and GG are distinct from air ($^{20}Ne/^{22}Ne_{AIR} = 9.80$; $^{21}Ne/^{22}Ne_{AIR} = 0.0290$; Ozima and Podosek, 1983), considering 1σ analytical uncertainties (Figs. 3 and S2). PAVF and GG peridotites are characterized by high $^{21}Ne/^{22}Ne$ relative to the MORB trend for a given $^{20}Ne/^{22}Ne$, which indicates

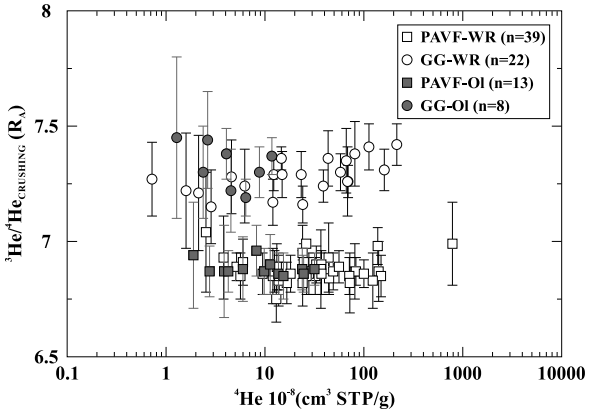

Fig. 2. Relationship between $^3He/^4He$ (in R_A, where 1 R_A corresponds to the atmospheric ratio of 1.4×10^{-6}; Ozima and Podosek, 1983) and the total ^4He concentration (in 10^{-8} cm^3 STP/g) obtained by crushing extraction. Uncertainties are 1σ; only crushing experiments are reported. WR = whole-rock (PAVF = open square; GG = open circle), Ol = olivine (PAVF = grey square; GG = grey circle).

endmembers more nucleogenic than a global MORB source. The mixing lines between a mantle endmember and atmospheric composition define MORB-like and more nucleogenic mantle reservoirs in the neon three-isotope diagram (Figs. 3 and S2). It is important to note that coupled crushing/heating experiments carried out on samples from PAVF showed similar results for neon (Fig. 3A and Supplementary Tables S2–S3). Therefore, we adopted all heating and crushing experiments to constrain the PAVF noble gas mantle source. However, except for samples PM23–1, PM23–11, PM23–14, and PM23–32, anomalous heating neon data from GG were observed. These results are not considered for further discussion because of in situ nucleogenic production by reaction of alpha-particles produced from the decay of U- and Th-series elements with oxygen in the mineral lattice was possible.

Well-defined linear trends in the neon three-isotope diagram (Figs. 3 and S2) were used to extrapolate the mantle source $^{21}Ne/^{22}Ne$ (hereafter referred to as $^{21}Ne/^{22}Ne_{(E)}$) of each studied mantle xenolith at $^{20}Ne/^{22}Ne = 12.5$ (Ne–B; Trieloff et al., 2000) with high reliability. The extrapolated $^{21}Ne/^{22}Ne$ ratios were determined by x and y error weighted least squares regression forced through the atmospheric composition [$y = a_0(x - 0.029) + 9.8$]. Mantle xenoliths from PAVF show a $^{21}Ne/^{22}Ne_{(E)}$ ratio, corrected for atmospheric contamination, ranging from 0.085 ± 0.001 (PM18–35WR) to 0.094 ± 0.003 (PM14–15Ol) and $PAVF_{AVERAGE}$ of 0.090 ± 0.002. As an exception among PAVF samples, sample PM14–4 shows a low $^{21}Ne/^{22}Ne_{(E)}$ value of 0.071 ± 0.001. Conversely, the $GG_{AVERAGE}$ is characterized by $^{21}Ne/^{22}Ne_{(E)} = 0.077 \pm 0.001$ whereas the sample PM23–1 shows the lowest $^{21}Ne/^{22}Ne_{(E)}$ value among all samples, at 0.065 ± 0.002. The extrapolated $^{21}Ne/^{22}Ne$ ratios of the PAVF samples are significantly more nucleogenic than MORB ($^{21}Ne/^{22}Ne_{(E)} = 0.060$; Sarda et al., 1988; Moreira et al., 1998), European SCLM ($^{21}Ne/^{22}Ne_{(E)} = 0.071$; Buikin et al., 2005), and Mangaia HIMU ($^{21}Ne/^{22}Ne_{(E)} = 0.077$; Hanyu et al., 2011) endmembers. Based on this comparison, it is possible to conclude that $PAVF_{SCLM}$ is characterized by neon that is far more nucleogenic than the previously defined endmembers.

The trend of one exceptional sample from GG (PM23–1) is indistinguishable from that of NCR MORBs ($^{21}Ne/^{22}Ne_{(E)} = 0.063$;

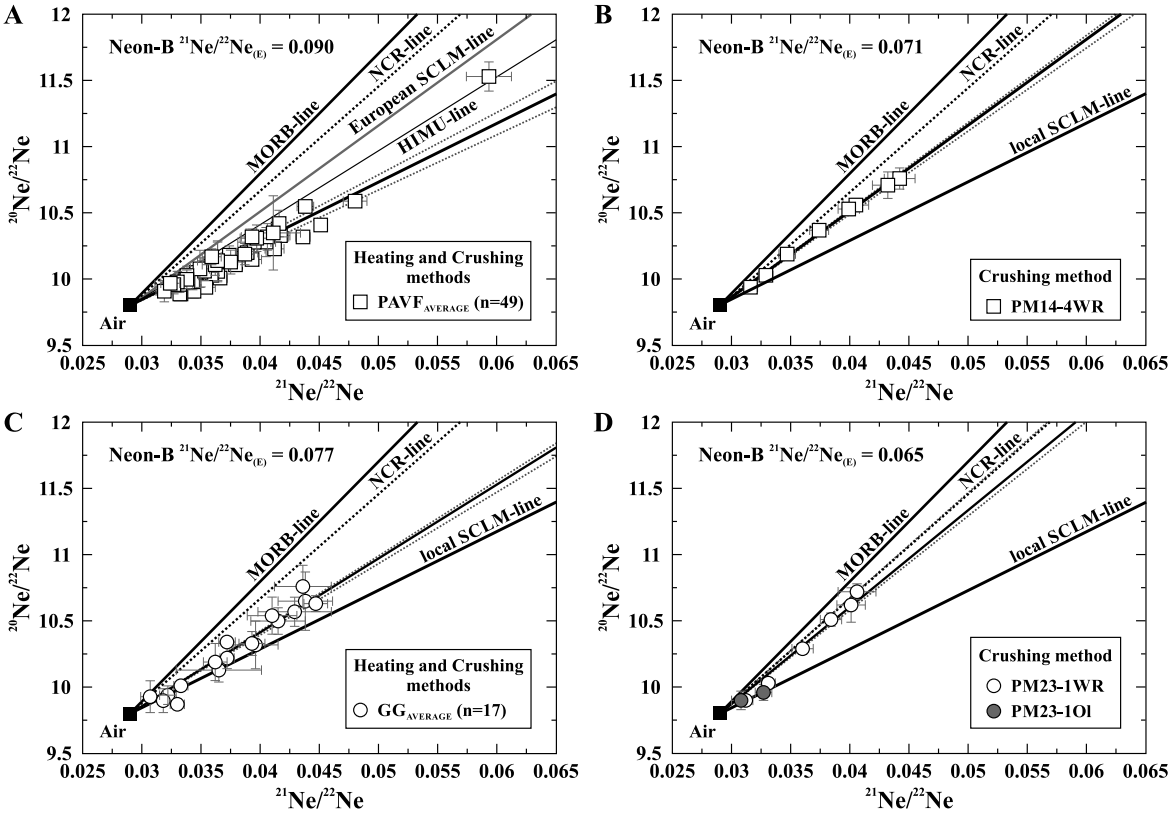

Fig. 3. Neon three-isotope diagram showing all individual single step heating and stepwise crushing results of PAVF and GG that differ from air with analytical uncertainties of 1σ. In some cases, the uncertainties are smaller than the symbol size. We calculated the trend line by applying data regression including an air data point and using uncertainties as weight. Well-defined lines by the data in (A)–(D) indicate a mixing of air with each mantle component, (A) for local SCLM, (B) for sample PM14–4, (C) for $GG_{AVERAGE}$, and in (D) for local MORB-like component (equivalent to NCR) observed in sample PM23–1. The data in (B) and (C) deviate from the lines defined by data in (A) and (D), indicating that their mantle components have distinctive compositions but can be accounted for by a mixing of the two endmembers, local SCLM and a MORB-like components. See text for references.

Niedermann and Bach, 1998) considering the analytical uncertainties; therefore, this sample represents a local MORB-like neon component (Fig. 3D). Consequently, the other peridotites from GG, as well as sample PM14–4 (PAVF), can be accounted for by three-component mixing between an atmospheric component and two mantle endmembers: MORB-like and a more radiogenic/nucleogenic SCLM components (Figs. 3 and S2).

4.3. Heavy noble gases

The $^{40}Ar/^{36}Ar$ ratios obtained by heating and crushing extractions range from 380 to 4830 in GG and from 420 to 17700 in PAVF peridotites (Supplementary Tables S2–S3). The values close to the atmospheric ratio (296; Ozima and Podosek, 1983), particularly those from GG peridotites, indicate atmospheric contamination. This probably occurred during exposure on the surface and/or could be associated with the recycled oceanic lithosphere in the Patagonian SCLM. The highest $^{40}Ar/^{36}Ar$ ratios determined in this study were obtained in sample PM14–4 ($^{40}Ar/^{36}Ar_{HEATING} = 17700 \pm 160$; $^{40}Ar/^{36}Ar_{CRUSHING} = 16400 \pm 120$), which implies a relatively small contribution of atmospheric argon. Our results are similar to the highest $^{40}Ar/^{36}Ar$ values measured in a mantle xenolith from European SCLM at 16200 ± 200 (Buikin et al., 2005). However, all measured $^{40}Ar/^{36}Ar$ ratios are significantly lower than the highest $^{40}Ar/^{36}Ar$ ratio reported for mantle xenoliths from Saudi Arabia at 25590 ± 620 (Hopp et al., 2007), and those found in MORBs, which range from ~28000 to 42000 (e.g., Moreira et al., 1998; Tucker et al., 2012). Considering that $^{40}Ar/^{36}Ar$ ratios represent mixing between mantle sources and an atmospheric component, we can infer the mantle source composition only by using neon–argon isotope correlations, which are presented in section 5.3.

The krypton isotopic ratios determined by crushing experiments are listed in Supplementary Table S4. All measured isotopic ratios are indistinguishable from atmospheric compositions at analytical uncertainties of 1σ.

The xenon isotopic data were also obtained by crushing and are presented in Supplementary Table S5. Xenon isotopic ratios for some samples from GG (PM23–1 and PM23–32) and PAVF (PM14–4, PM14–15, PM18–23, and PM18–35) are clearly distinguishable from those of air with analytical uncertainties of 1σ [$^{129}Xe/^{132}Xe_{AIR} = 0.9832$; $^{136}Xe/^{132}Xe_{AIR} = 0.3294$; Ozima and Podosek (1983)]. In the three-isotope diagram of $^{129}Xe/^{132}Xe$ versus $^{136}Xe/^{132}Xe$ (Figs. 4 and S3), Patagonian mantle xenoliths define a correlation line indistinguishable from the mixing line between air and depleted MORB (e.g., Kunz et al., 1998; Tucker et al., 2012).

4.4. Sr–Nd–Pb isotopes

In this section, we report new Sr–Nd–Pb isotopic data and radiometric ages for the same whole-rock suite and mineral separates for which we have presented the noble gas data above (Supplementary Table S6). The Sr–Nd–Pb isotopic compositions of both suites are highly similar, with $^{87}Sr/^{86}Sr = 0.702811$–$0.703259$, $^{143}Nd/^{144}Nd = 0.512847$–$0.512993$, $^{206}Pb/^{204}Pb = 17.99$–$19.09$. These results are in agreement with those previously reported by Stern et al. (1999), and Gorring and Kay (2000) for samples from the same localities. The Sr–Nd isotopic signature of PAVF and GG xenoliths requires a depleted component because they plot between Chile Ridge MORBs (Klein and Karsten, 1995; Bach et al., 1996) and HIMU–OIBs (high $^{238}U/^{204}Pb$; Fig. 5A). The lead isotope ratios for PAVF and GG overlap with the field of Chile Ridge MORBs (Klein and Karsten, 1995; Bach et al., 1996), with significantly lower $^{206}Pb/^{204}Pb$ ratios than the HIMU endmember (Fig. 5B). Our samples display some affinity to HIMU with respect to noble gases as discussed in sections 5.1 and 5.2, such as slightly radiogenic helium and strongly nucleogenic neon. However, the less-radiogenic lead isotopic ratios than those observed in this mantle reservoir [e.g., $^{206}Pb/^{204}Pb > 20.5$; Hanyu et al., 2014] serve as evidence against the contribution of this component in the SCLM beneath PAVF and GG (Fig. 5B).

Additionally, the formation age of phlogopite, which is a key mineral for determining the time of the metasomatic imprint and its potential association with geotectonic events, was calculated by using an Rb–Sr isochron including whole-rock, clinopyroxene and

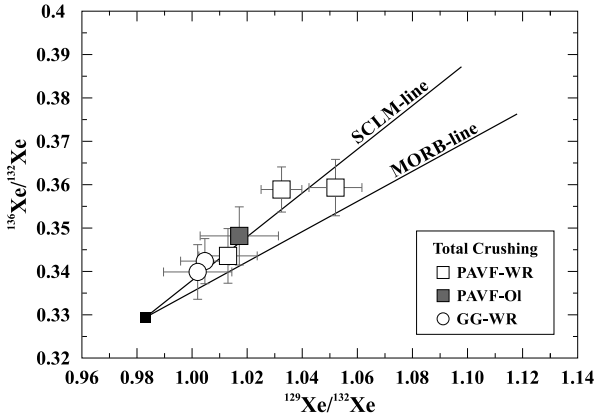

Fig. 4. Plot of $^{129}Xe/^{132}Xe$ versus $^{136}Xe/^{132}Xe$ ratios of total crushing for PAVF and GG peridotites. Data that differ by 1σ from atmospheric ratios are shown; uncertainties are 1σ. WR = whole-rock (PAVF = open square; GG = open circle), Ol = olivine (PAVF = grey square). See text for references.

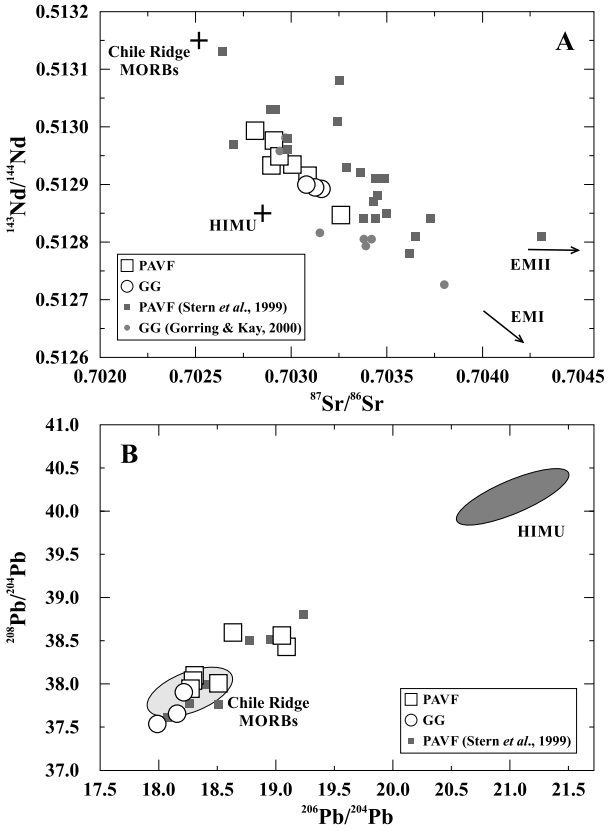

Fig. 5. (A) $^{87}Sr/^{86}Sr$ versus $^{143}Nd/^{144}Nd$ and (B) $^{206}Pb/^{204}Pb$ versus $^{208}Pb/^{204}Pb$ isotope variations of whole-rock and mineral separates from selected PAVF and GG peridotites. For comparison, data from HIMU (Hanyu et al., 2011, 2014), PAVF (Stern et al., 1999), GG (Gorring and Kay, 2000), and Chile Ridge MORBs [NCR from Bach et al. (1996) and SCR from Klein and Karsten (1995)] are also plotted. The mantle reservoirs are from Hart et al. (1992).

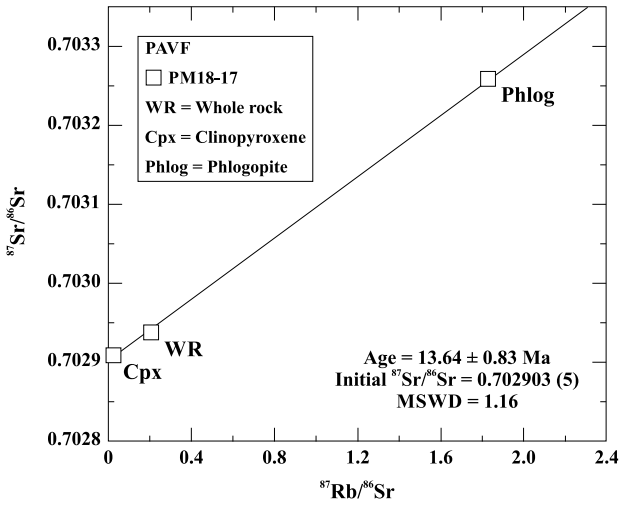

Fig. 6. Rb–Sr mineral isochron for a garnet-spinel harzburgite from PAVF (PM18–17). The uncertainties are 1σ of the mean, corresponding to last digit of the $^{87}Sr/^{86}Sr$ ratio. The 1σ uncertainties are smaller than the size of the symbols.

phlogopite data of a PAVF sample (PM18–17). The obtained age is 13.64 ± 0.83 Ma with initial $^{87}Sr/^{86}Sr = 0.702903 \pm 0.000005$ (2σ) (MSWD = 1.16; Fig. 6). This age suggests concomitant formation of phlogopite with subduction and dehydration of the southeast extension of the Chile Ridge (SCR–3) ca. 14–13 Ma ago (e.g., Cande and Leslie, 1986; D'Orazio et al., 2000). It is unclear at present if the metasomatic event resulting in high $(U+Th)/(^{3}He, ^{22}Ne)$ ratios of PAVF samples corresponds to or predates that constrained by the Rb–Sr system because unfortunately, the noble gas concentrations of sample (PM18–17) were too low to constrain the mantle $^{3}He/^{4}He$ and $^{21}Ne/^{22}Ne_{(E)}$ features.

5. Discussion

5.1. Slab-derived metasomatism or in situ radiogenic/cosmogenic contributions on helium isotopes?

Post-eruptive processes that can affect the $^{3}He/^{4}He$ ratios are: 1) cosmogenic ^{3}He by $^{6}Li(n,\alpha)^{3}H(\beta^{-})^{3}He$ reaction, which is induced by thermalized neutrons, resulting either from U–Th decay and subsequent (α, n) reactions within rocks or from secondary cosmic ray cascades in the atmosphere and in rocks; and 2) radiogenic ingrowth of ^{4}He by alpha decay of uranium and thorium. In order to separate a mantle fluid component from possible in situ radiogenic or cosmogenic contributions, results from both crushing and heating experiments are compared. It is generally assumed that gas extracted dominantly from fluid inclusions by crushing is less affected by cosmogenic and radiogenic helium (^{3}He and ^{4}He, respectively), which occurs mainly in the mineral lattice, and only a small amount can be transferred to fluid inclusions. As a result, helium isotopic ratios observed in the heating experiments that are lower or higher than the range defined by using the crushing method likely reflect radiogenic ^{4}He or cosmogenic ^{3}He production (e.g., Kurz, 1986). The observed $^{3}He/^{4}He$ ratios for PAVF and GG xenoliths obtained by heating extraction show significant dispersion (3.60–10.38 R_A; Supplementary Tables S2–S3). On the contrary, when analyzed by crushing extraction, the $^{3}He/^{4}He$ ratios are uniform ($^{3}He/^{4}He_{PAVF} = 6.84$–$6.90$ R_A; $^{3}He/^{4}He_{GG} = 7.17$–$7.37$ R_A) (Figs. 2 and S1). Two samples of GG (8.18–8.36 R_A) and eighteen samples of PAVF (7.10–10.38 R_A) analyzed by heating have higher $^{3}He/^{4}He$ ratios than those obtained by crushing (Supplementary Tables S2–S3). In contrast, all wehrlites (3.60–4.82 R_A) and one lherzolite (5.45 R_A; PM23–2) of GG analyzed by heating extraction show lower $^{3}He/^{4}He$ ratios than the range of GG samples obtained by crushing (7.17–7.37 R_A; Figs. 2 and S1). To verify whether the lower $^{3}He/^{4}He$ ratios of some GG peridotites are related to the post-eruption production of ^{4}He, we compare the $^{3}He/^{4}He$ ratios obtained by stepwise crushing and single step heating using sample PM23–34. This sample has a low $^{3}He/^{4}He$ ratio (4.18 R_A) when analyzed by the heating method; however, when analyzed by the crushing method, it shows higher $^{3}He/^{4}He = 7.21$ R_A (Supplementary Tables S2–S3). These observations clearly indicate that helium is more affected by radiogenic ^{4}He or by cosmogenic ^{3}He in the matrix than that in the fluid inclusions. Therefore, in this study we assumed that the $^{3}He/^{4}He$ ratios obtained by crushing represent the SCLM beneath PAVF and GG. Moreover, no systematic difference in noble gas isotopes was found between olivine and the whole-rock samples analyzed by the crushing method, which indicates that our whole-rock results represent noble gas compositions in the mantle source.

The representative $^{3}He/^{4}He$ ratios of the PAVF peridotites overlap the values defined around the world as SCLM (6.1 ± 2.1 R_A; Day et al., 2015) and HIMU-like mantle source ($^{3}He/^{4}He = 5$–7 R_A; e.g., Moreira and Kurz, 2001). However, the values obtained for GG peridotites overlap the field defined as global MORBs (8 ± 1 R_A; Sarda et al., 1988; Moreira et al., 1998) and are similar to the North Chile Ridge (NCR) MORBs (7.77 ± 0.23 R_A; Niedermann and Bach, 1998).

In general, fluids and/or melts can be produced by dehydration and/or melting of the slab in the mantle beneath the subduction zone. Radiogenic helium with low $^{3}He/^{4}He$, produced by the decay of uranium and thorium (and lithium), accumulates in sources of fluids/melts, such as sediments and altered oceanic crust. Sumino et al. (2010) reported that slab-derived, water-rich fluid trapped in mantle wedge peridotite just above the subducting slab exhibits lower $^{3}He/^{4}He$ than the MORB source, because of radiogenic helium from the slab mixing with mantle-derived helium. In contrast, even the highest $^{3}He/^{4}He$ ratios from island arc segments, which contain a significant volume of subducting sediments and/or old oceanic crust (e.g., the Aleutian Islands and Izu–Mariana arc), are almost equivalent to that of MORB source mantle (Hilton et al., 2002). Low $^{3}He/^{4}He$ ratios typically found in arcs with thick continental crust are considered the result from crustal contamination of helium at shallower depths (e.g., Hilton et al., 1993). This suggests that the radiogenic helium signature of slab-derived fluids was diluted by mantle-derived helium during fluid migration in the mantle wedge. As a result, slab-derived helium has rarely been observed where subduction of thick continental crust/oceanic plateau is ongoing (Sumino et al., 2004 and references therein). Alternatively, the systematically lower $^{3}He/^{4}He$ values of SCLM than the MORB value are generally attributed to a higher $(U+Th)/^{3}He$ ratio than the MORB source (e.g., Yamamoto et al., 2004; Gautheron et al., 2005; Kim et al., 2005; Barry et al., 2015; Day et al., 2015 and references therein). Although some of the low $^{3}He/^{4}He$ ratios associated with extremely high concentrations of ^{4}He could have resulted from the addition of radiogenic helium accompanying slab-derived metasomatic fluids (Barry et al., 2015; Day et al., 2015), the ^{4}He concentrations of our xenoliths are not high and no clear relationship is noted between the ^{4}He concentration and the $^{3}He/^{4}He$ ratio (Supplementary Table S2). This indicates an insignificant contribution of slab-derived radiogenic helium. Instead, the low $^{3}He/^{4}He$ ratios of peridotites from PAVF would have originated from time-integrated evolution in the SCLM containing a higher $(U+Th)/^{3}He$ ratio than the MORB source.

5.2. Helium–neon systematics

Because He–Ne isotope systematics are coupled (Honda et al., 1993), the increase in $^{21}Ne/^{22}Ne$ should be associated with a decrease in $^{3}He/^{4}He$ because of constant $^{21}Ne/^{4}He$ production in

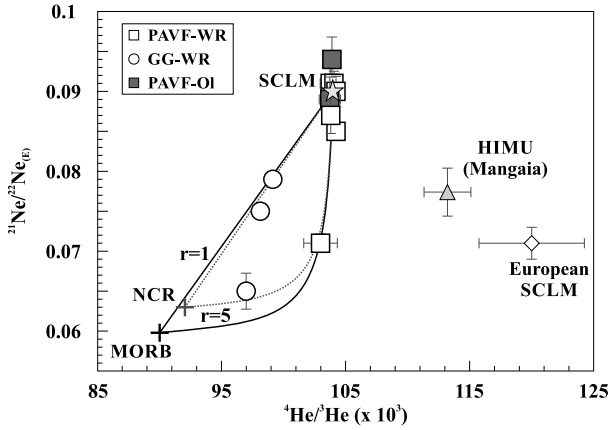

Fig. 7. $^{4}He/^{3}He$ versus $^{21}Ne/^{22}Ne_{(E)}$ for Southern Patagonia peridotites. The $^{21}Ne/^{22}Ne$ ratios were extrapolated to a mantle endmember value of $^{20}Ne/^{22}Ne = 12.5$ (Trieloff et al., 2000). To avoid in situ produced radiogenic/nucleogenic and cosmogenic effects, as well as elemental fractionation, only crushed samples are considered. Thus, $^{4}He/^{3}He$ and $^{21}Ne/^{22}Ne_{(E)}$ are the total crushing results for each sample that differ from air by 1σ. Uncertainties given correspond to 1σ. In some cases, uncertainties are smaller than the symbol size. The He–Ne relationship can be explained by the mixing lines between MORBs and the assumed local SCLM endmembers. Mixing lines are presented for r ranging from 1 to 5, where $r = (^{3}He/^{22}Ne)_{SCLM}/(^{3}He/^{22}Ne)_{MORB}$. For comparison, European SCLM (sample DW1; Buikin et al., 2005) and Mangaia HIMU (Hanyu et al., 2011) reservoirs are plotted.

the mantle (4.5×10^{-8}; Yatsevich and Honda, 1997). Although the helium isotopic characteristics of $PAVF_{SCLM}$, which is only slightly more radiogenic than the MORB source, suggests apparent decoupling between the helium and neon isotope systematics, it can be accounted for by the higher $^{3}He/^{22}Ne$ ratio of the $PAVF_{SCLM}$ than the MORB source and other SCLMs. The $^{4}He/^{3}He$ and $^{21}Ne/^{22}Ne_{(E)}$ isotopic ratios of GG and PAVF peridotites can be explained by a binary mixing hyperbola between MORB and an even more degassed SCLM (radiogenic/nucleogenic) components (Fig. 7). Here, we assume that local SCLM is represented by the data of PAVF mantle xenoliths ($^{21}Ne/^{22}Ne_{(E)} = 0.090$; $^{4}He/^{3}He = 104000$), as they are most radiogenic/nucleogenic among all samples, whereas the MORB sources used in the modeling are global ($^{21}Ne/^{22}Ne_{(E)} = 0.060$; $^{4}He/^{3}He = 90000$; Sarda et al., 1988; Moreira et al., 1998) and NCR MORBs ($^{21}Ne/^{22}Ne_{(E)} = 0.063$; $^{4}He/^{3}He = 92000$; Niedermann and Bach, 1998). The equation employed for the mixing hyperbola is from Hopp and Trieloff (2008), where a straight line indicates equal $^{3}He/^{22}Ne$ ratios [$r = 1$, where $r = (^{3}He/^{22}Ne)_{SCLM}/(^{3}He/^{22}Ne)_{MORB}$], whereas a hyperbolic mixing line ($r = 5$) signifies different helium and neon contributions from each endmember.

In order to avoid the influence of shallow level air contamination in the $^{3}He/^{22}Ne$ ratios (Supplementary Table S7), we calculated a mantle source value in the studied xenoliths from the measured helium and neon isotope ratios following the method proposed by Honda and McDougall (1998) as follows:

$$^{3}He/^{22}Ne = \frac{^{21}Ne/^{22}Ne_{(E)} - ^{21}Ne/^{22}Ne_{(I)}}{^{4}He/^{3}He - ^{4}He/^{3}He_{(I)}} \times (^{4}He/^{21}Ne)^{*}_{production}$$

For calculations, we used the $^{4}He/^{3}He$ and $^{21}Ne/^{22}Ne_{(E)}$ ratios of each sample, as well as $(^{4}He/^{21}Ne)^{*}_{production}$ of 2.2×10^{7} (Yatsevich and Honda, 1997), the initial primordial composition of $^{21}Ne/^{22}Ne$ ($^{21}Ne/^{22}Ne_{(I)} = 0.0313$; Trieloff and Kunz, 2005) and $^{4}He/^{3}He$ ($^{4}He/^{3}He_{(I)} = 6024$ or $^{3}He/^{4}He_{(I)} = 120$ R_A; Mahaffy et al., 1998). The uncertainties in $^{3}He/^{22}Ne$ were propagated from uncertainties in $^{4}He/^{3}He$ and $^{21}Ne/^{22}Ne_{(E)}$.

The $^{3}He/^{22}Ne$ values for the $PAVF_{SCLM}$ endmember show higher ratios (12.03 ± 0.15 to 13.66 ± 0.37) than those in the depleted MORBs ($^{3}He/^{22}Ne = 8.31$–9.75; Tucker et al., 2012). The local MORB-like component, which exhibits an almost identical $^{21}Ne/^{22}Ne_{(E)}$ ratio as that of NCR MORBs (Fig. 3D) in GG (PM23–1; $^{3}He/^{22}Ne = 8.39 \pm 0.14$), and sample PM14–4 (PAVF; $^{3}He/^{22}Ne = 9.01 \pm 0.17$) shows values over the range of depleted MORBs; other samples from GG vary between 10.44 ± 0.11 and 11.27 ± 0.12. The significantly higher $^{3}He/^{22}Ne$ ratios observed in the $PAVF_{SCLM}$ samples, compared with those in the MORB component, may represent mantle heterogeneity.

Comparatively, even if the He–Ne component of $PAVF_{SCLM}$ is less radiogenic in helium isotopes, it is more nucleogenic in neon than Mangaia HIMU ($^{4}He/^{3}He = 113200$, $^{21}Ne/^{22}Ne_{(E)} = 0.077$; Hanyu et al., 2011), as well as than European (DW1 sample with $^{4}He/^{3}He = 120000$, $^{21}Ne/^{22}Ne_{(E)} = 0.070$; Buikin et al., 2005) and Arabic (SA86–121/1 sample with $^{4}He/^{3}He = 116000$, $^{21}Ne/^{22}Ne_{(E)} = 0.070$; Hopp et al., 2004) SCLMs (also see sections 4.2 and 5.1). Moreover, the calculated $^{3}He/^{22}Ne$ ratios for Mangaia HIMU (9.38), as well as for the European (7.47) and Arabic SCLMs (7.74), are significantly lower than those found in the Patagonian SCLM. This suggests that the Patagonian SCLM experienced a different evolution from a MORB source and other SCLMs. Our preferred model for explaining the higher $^{3}He/^{22}Ne$ ratios observed in Patagonian SCLM is based on the greater compatibility of helium compared with neon, which resulted in an increase in the $^{3}He/^{22}Ne$ ratio of the mantle during depletion of these peridotites due to melt extraction (e.g., Niedermann and Bach, 1998; Hopp and Trieloff, 2008). Although it is not well experimentally constrained whether there is a clear difference in compatibility between helium and neon during melt extraction (e.g., Heber et al., 2007), relative enrichment of helium to neon has been invoked to explain helium deficit of plume-derived magma (Hopp and Trieloff, 2008). Considering that PAVF mantle xenoliths migrated back and forth between the lithosphere and asthenosphere by a few tens of kilometers over time (e.g., Stern et al., 1999), we suggest that these samples experienced low partial melting degree through a vertical delamination process. As a result, the neon isotopic ratios could have been modified more readily than helium owing to the lower neon content in a previously degassed mantle reservoir. Thus, the $^{3}He/^{4}He$ ratios would decrease and $^{21}Ne/^{22}Ne$ ratios would increase in the residue after degassing.

Asthenospheric mantle upwelling through the Patagonian slab window would result in a slightly metasomatized $PAVF_{SCLM}$ with a MORB-like signature after collision of the SCR with the Chile trench ca. 14 Ma, which would imply less radiogenic/nucleogenic isotopic ratios of $^{4}He/^{3}He$ and $^{21}Ne/^{22}Ne$. We suggest that this metasomatism was unable to completely overprint the noble gas composition of PAVF mantle xenoliths because of rapid northward migration of the CTJ. This is supported by the observation that most of the PAVF samples preserved the SCLM composition during mixing (Fig. 7). As an exception, sample PM14–4 plots along the hyperbolic mixing curve ($r = 5$) and shows helium isotopic ratios of the intrinsic SCLM, whereas their neon is affected by a MORB-like component. This sample is significantly enriched in helium by a factor of more than 10 times that of neon (Supplementary Table S3). As shown above, the $^{3}He/^{22}Ne$ ratio of the SCLM endmember is only approximately 40% higher than that of the MORB source. This indicates that the metasomatic input with MORB-like helium and neon isotopic compositions was paradoxically also enriched in helium derived from the SCLM. Although we have no convincing explanation for this particular sample at present, we speculate that complicated metasomatism processes resulted in a concentration of SCLM-type noble gases in a small proportion of the SCLM, especially highly diffusive helium followed by addition of MORB-like noble gases brought by the upwelling asthenosphere.

In contrast, the helium in SCLM was likely diluted or homogenized during the last 14 Ma (see details about the Rb–Sr

isochron in section 4.4) because it is more diffusive than neon and could therefore be easily homogenized. Similarly, PM23–1 (GG) xenolith data also plots along the same hyperbola ($r = 5$). However, this sample shows lower radiogenic/nucleogenic $^{4}He/^{3}He$ and $^{21}Ne/^{22}Ne_{(E)}$ isotopic ratios, suggesting that it is largely dominated by a MORB-like component, especially when compared to NCR MORBs. Two samples from GG (PM23–32 and PM23–34) plot close to the mixing line between SCLM and MORB endmembers [$(^{3}He/^{22}Ne)_{SCLM}/(^{3}He/^{22}Ne)_{MORB} = 1$)], owing to the different contributions of the MORB-like component in the Patagonian SCLM. Therefore, we argue that the less radiogenic/nucleogenic MORB-like component identified in the GG samples could be explained by recent metasomatism of the SCLM from asthenospheric mantle upwelling in response to opening of the Patagonian slab window, which is a consequence of SCR subduction. Contrary to the findings of Barry et al. (2015), that such metasomatic input of noble gases can be detected as absolute concentration enrichments, there is no systematic helium enrichment in the GG samples compared to the PAVF samples (Fig. 2). The concentrations of crush-released helium (Supplementary Table S2) range from 15% to 102% of those obtained after heating the same sample (Supplementary Table S3), suggesting that the noble gas concentrations in our samples are strongly controlled by the number density of fluid inclusions. Because the number density of the inclusions is not always dependent on the metasomatic process, the absolute noble gas concentrations in our samples do not differ systematically between GG and PAVF.

5.3. Argon–neon systematics

In general, mixing between isotopic ratios with different denominators is represented by hyperbolas. In Ar–Ne systematics, the curvature of the two endmembers hyperbola is defined by $r = (^{36}Ar/^{22}Ne)_A/(^{36}Ar/^{22}Ne)_B$ (e.g., Hopp et al., 2007; Parai et al., 2012). However, when the $^{36}Ar/^{22}Ne$ values of each sample obtained by dividing their total ^{36}Ar by total ^{22}Ne concentrations are similar to the atmospheric ratio (18.7; Ozima and Podosek, 1983) (see Supplementary Table S7), it is reasonable to assume linear mixing [$(^{36}Ar/^{22}Ne)_{MANTLE}/(^{36}Ar/^{22}Ne)_{AIR} = 1$] (Sumino et al., 2006).

Except for samples PM14–4 ($^{36}Ar/^{22}Ne = 3.29 \pm 0.02$) and PM23–1 ($^{36}Ar/^{22}Ne = 9.96 \pm 0.06$), most xenoliths show similar $^{36}Ar/^{22}Ne$ ratios to air (14.76 ± 0.09 to 25.56 ± 0.13) (Supplementary Table S7). Thus, we restricted hyperbolic extrapolations to samples that differ significantly from air in terms of $^{36}Ar/^{22}Ne$ ratios, specifically PM14–4 and PM23–1 (Figs. 8 and S4).

In order to obtain the best-fit hyperbola reflecting two-component mixing between air and mantle endmembers, we applied the approach proposed by Parai et al. (2012). This method consists of a total least-squares hyperbolic fit, where the fit process is based on chi-square statistics computed by using the orthogonal error weighted distances and a Markov Chain Monte Carlo (MCMC) optimization. This method uses a hyperbola with two free parameters to fit the data. The first describes the curvature of the model (r), and the second is the model value at a fixed value in the abscissa (Neon–B $^{20}Ne/^{22}Ne = 12.5$). Moreover, the model forces the best-fit hyperbola to pass through the atmospheric composition. In this modeling, as well as to determine the $^{36}Ar/^{22}Ne$ values, we used all argon isotopic data that correspond with the selected neon results. It should be noted that the two samples to which the hyperbola fitting were applied are also accounted for by a hyperbolic mixing in the He–Ne system (Fig. 7). Therefore it is speculated that noble gases in the mantle domains where these samples are derived from might be fractionated during mixing between the local SCLM and MORB-like components resulting in different r values from those for other South Patagonian samples, MORBs, and European SCLM (Figs. 8 and S4). Alternatively, because the observed $^{36}Ar/^{22}Ne$ ratios of these samples are lower than the atmospheric value, the atmospheric contaminant could be highly fractionated to have lower $^{36}Ar/^{22}Ne$ ratio than the original value, which is similar to those observed in European SCLM (Buikin et al., 2005). However, there is no plausible explanation for the moment.

By extrapolating regression lines to Neon–B $^{20}Ne/^{22}Ne = 12.5$, we found $^{40}Ar/^{36}Ar_{(E)}$ ratios for intrinsic $PAVF_{SCLM}$ over a range of 31100^{+9400}_{-6800} to 54000^{+14200}_{-9600} (Figs. 8 and S4). This interval is in agreement with that proposed for European SCLM ($^{40}Ar/^{36}Ar =$ 34000–52000; Buikin et al., 2005) and is substantially higher than the "popping rock" sample 2*Π*D43 (25000; Moreira et al., 1998) and the MORB reservoir (41500 ± 9000; Tucker et al., 2012). In order to compare previous data with the best-fit hyperbola using our approach, we fitted the $^{40}Ar/^{36}Ar_{(E)}$ to the "popping rock" sample (25700^{+1200}_{-1100}; Moreira et al., 1998), sample DW1 from European SCLM (13400^{+4900}_{-2300}; Buikin et al., 2005), and a depleted MORB sample RC28063D–2 (38600 ± 350; Tucker et al., 2012) (Fig. S4).

The high $^{40}Ar/^{36}Ar_{(E)}$ observed in the Patagonian SCLM endmember implies an even more degassed reservoir than a MORB source with a high $K/^{36}Ar$ ratio, accompanied by high $(U + Th)/(^{3}He, ^{22}Ne)$ isotopic ratios. However, the GG mantle xenoliths show $^{40}Ar/^{36}Ar_{(E)}$ between 8100^{+1400}_{-700} and 17700^{+4400}_{-3100}, which are lower than those observed in PAVF samples, implying a significant contribution from atmospheric argon. This could indicate effective recirculation of atmospheric argon associated with recycled oceanic lithosphere in the Patagonian SCLM, as observed in xenoliths from subduction zones (e.g., Matsumoto et al., 2001; Kim et al., 2005; Sumino et al., 2010; Hopp and Ionov, 2011).

5.4. Xenon isotopes

The best-fit hyperbola for xenon mantle compositions was obtained by using the same approach for argon as described above (see section 5.3 for further details). Despite a limited number of data points, it was possible to extrapolate xenon isotope ratios for samples PM14–4 ($^{129}Xe/^{132}Xe_{(E)} = 1.0833^{+0.0216}_{-0.0053}$; $^{136}Xe/^{132}Xe_{(E)} = 0.3761^{+0.0246}_{-0.0034}$) and PM14–15 ($^{129}Xe/^{132}Xe_{(E)} = 1.0556^{+0.0614}_{-0.0040}$; $^{136}Xe/^{132}Xe_{(E)} = 0.3720^{+0.0401}_{-0.0056}$) (Figs. 9 and S5). It should be noted that this is the first SCLM xenon isotope composition defined from any mantle xenoliths. For consistent comparison, we applied the same approach again to fit the xenon isotopic composition of sample RC28063D–2, which was assumed to be representative of the depleted MORB mantle group (Tucker et al., 2012). These extrapolations yielded a mantle source $^{129}Xe/^{132}Xe = 1.1156^{+0.0442}_{-0.0124}$ and $^{136}Xe/^{132}Xe = 0.3850^{+0.0156}_{-0.0061}$, which is consistent with the previously estimated values of $^{129}Xe/^{132}Xe = 1.1180$ and $^{136}Xe/^{132}Xe = 0.3851$ (Fig. S5).

If the Patagonian SCLM experienced noble gas degassing and/or metasomatic uranium input, $^{129}Xe/^{132}Xe_{(E)}$ would be lower than the MORB mantle whereas $^{136}Xe/^{132}Xe_{(E)}$ would be higher because ^{132}Xe and ^{136}Xe are produced by spontaneous fission of ^{238}U with a higher $^{136}Xe/^{132}Xe$ ratio (ca. 1.7, Ozima and Podosek, 1983) than the present-day MORB mantle value. Conversely ^{129}I, the parent isotope of ^{129}Xe, is extinct owing to its short half-life (16 Ma), thus there is no more production of ^{129}Xe. Alternatively, if the Patagonian SCLM includes a subducted atmospheric influence, $^{129}Xe/^{132}Xe_{(E)}$ and $^{136}Xe/^{132}Xe_{(E)}$ would be lower than MORB values. However, we can infer that Patagonian SCLM shows at least a similar excess of ^{129}Xe and ^{136}Xe to that of the MORB reservoir because of the very limited number of samples yielding mantle xenon isotope ratios and the large uncertainties accompanying the estimated ratio. The r values greater than unity indicate a higher $^{132}Xe/^{22}Ne$ ratio of the mantle endmember than that of

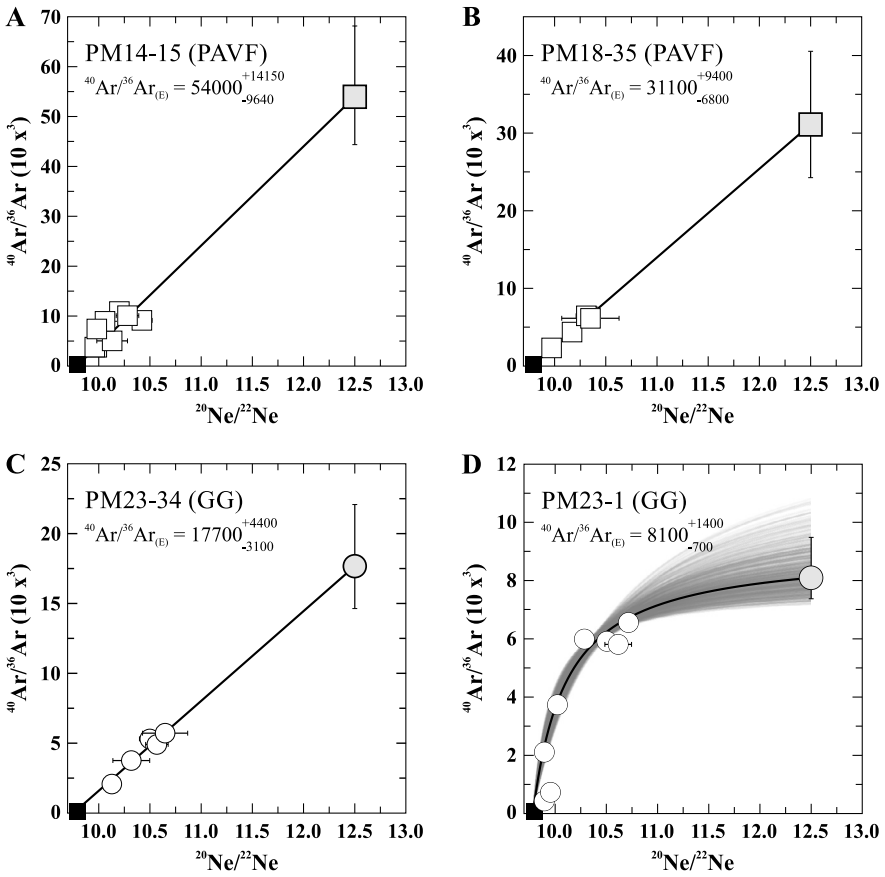

Fig. 8. Ar–Ne isotope systematics corrected for shallow-level air contamination. For each sample, stepwise crushing generates an array reflecting variable degrees of atmospheric contamination. For samples with a well-defined mixing array, we calculated the best-fit to extrapolated mantle $^{40}Ar/^{36}Ar$ at $^{20}Ne/^{22}Ne = 12.5$. In order to determine the mantle source $^{40}Ar/^{36}Ar$, we applied two approaches (see text for more details). Grey lines show 100 models randomly sampled from the chi-squared distribution up to 3σ from the best-fit model. It is also important to note that large uncertainties observed in extrapolated $^{40}Ar/^{36}Ar$ ratios are related to significant air contribution in both $^{40}Ar/^{36}Ar$ and $^{20}Ne/^{22}Ne$ ratios, which fall rather close to the air.

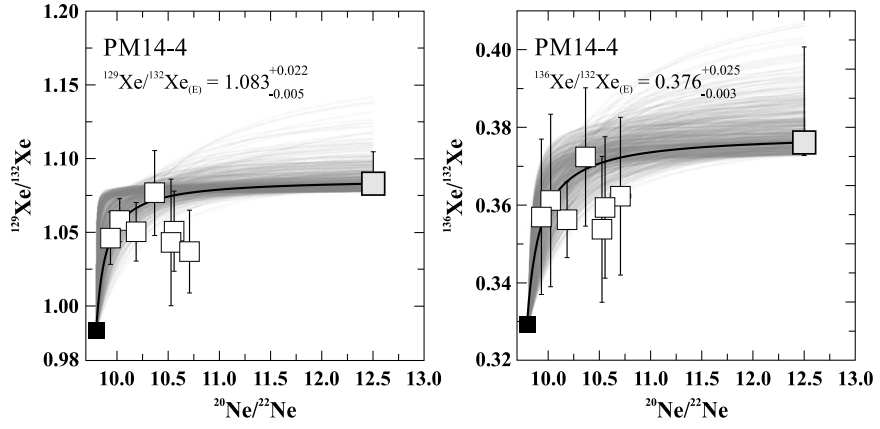

Fig. 9. Xe–Ne mixing systematics for sample PM14–4. Best-fit hyperbolae for this sample yielded an extrapolated mantle $^{129-136}Xe/^{132}Xe_{(E)}$ at $^{20}Ne/^{22}Ne = 12.5$. See the text for approach to fit the xenon isotopic composition of our sample. Grey lines show 100 models randomly sampled from the chi-squared distribution up to 3σ from the best-fit model. Data that differ by 1σ from atmospheric ratios are shown and uncertainties are 1σ.

atmospheric component, which is in clear contrast to the Xe–Ne systematics observed in MORBs (Figs. 9 and S5). However, the observed $^{132}Xe/^{22}Ne$ ratios of these samples, 0.0014 for PM14–4 and 0.0086 for PM14–15, are lower than that of unfractionated air at 0.014. This indicates the possibility that a fractionated atmospheric component mixed with an SCLM component indistinguishable from the MORB reservoir in terms of the $^{132}Xe/^{22}Ne$ ratio cannot be ruled out. Based on these results, we conclude that additional future measurements on these mantle xenoliths will be able to better constrain xenon ratios of the SCLM endmember.

6. Conclusions

We present the first noble gas data and new Sr–Nd–Pb isotopes of mantle xenoliths from the SCLM beneath southern Patagonia. Based on noble gas isotopic compositions determined by the stepwise crushing method we conclude that:

1) Heterogeneous SCLM beneath the PAVF and GG represents mixing between air and two mantle endmembers: one a degassed and depleted SCLM component with a radiogenic/nucleogenic composition and the other a MORB-like component.

2) Pali-Aike mantle xenoliths represent the intrinsic local SCLM reservoir with higher (U + Th + K)/(^{3}He, ^{22}Ne, ^{36}Ar) ratios than the MORB source, which would have remained unhomogenized during the last 14 Ma, after the rapid passage and northward migration of the CTJ and its slab window. This mantle reservoir is characterized by slightly radiogenic $^3He/^4He_{AVERAGE} = 6.87 \pm 0.04$ R_A, strongly nucleogenic mantle neon with a $^{21}Ne/^{22}Ne$ average of 0.090, and higher $^3He/^{22}Ne$ ratios (up to 13.66 ± 0.37) than depleted MORB source. The $^{40}Ar/^{36}Ar$ ratios vary from a near-atmospheric ratio of 510 up to 17700, with $^{40}Ar/^{36}Ar_{(E)}$ reaching 54000^{+14200}_{-9600}.

3) The less radiogenic/nucleogenic MORB-like component identified in the GG mantle xenoliths could be explained by recent metasomatism of the SCLM because of asthenospheric mantle upwelling in response to the opening of the Patagonian slab window, which is a consequence of SCR subduction. These xenoliths are characterized by $^3He/^4He_{AVERAGE} = 7.24 \pm 0.09$ R_A, and by slightly nucleogenic mantle neon with $^{21}Ne/^{22}Ne = 0.065$. $^{40}Ar/^{36}Ar$ ratios range between 380 and 6560 (usually less than 4000), with $^{40}Ar/^{36}Ar_{(E)}$ ranging between 8100^{+1400}_{-700} and 17700^{+4400}_{-3100}. This indicates that the mantle source of these rocks was significantly affected by atmospheric contamination, in terms of argon, associated with recycled oceanic lithosphere.

4) The $^{129-136}Xe/^{132}Xe$ isotopic ratios that are distinguishable from air with analytical uncertainties of 1σ form a mixing line between the air and MORB endmembers with $^{129}Xe/^{132}Xe_{(E)} = 1.0833^{+0.0216}_{-0.0053}$ and $^{136}Xe/^{132}Xe_{(E)} = 0.3761^{+0.0246}_{-0.0034}$. This suggests that Patagonian SCLM shows, at least, a similar excess of ^{129}Xe and ^{136}Xe to that of the MORB reservoir.

Acknowledgements

This study was supported by the National Council of Technological and Scientific Development – CNPq, Brazil (Project number 478632/2010-0), by the Graduate School of Science cooperative research program at the University of Tokyo, conceded to T.J., and by the Japan Society for the Promotion of Science (JSPS) Grant-in-Aid for Scientific Research (B) Nos. 23340169 and 26287139, the Sumitomo Foundation No. 100191, and Inamori Foundation conceded to H.S. We are thankful to G. Salerno for his help with mathematical models and to Prof. E. Koester and A. Martins for their support in Sr–Nd–Pb analysis. The authors are also grateful to Drs. J. Hopp and P. Barry for their thorough reviews and useful suggestions.

Appendix A. Supplementary material

Supplementary material related to this article can be found online at http://dx.doi.org/10.1016/j.epsl.2016.06.034.

References

Bach, W., Erzinger, J., Dosso, L., Bollinger, C., Bougault, H., Etoubleau, J., Sauerwein, J., 1996. Unusually large Nb–Ta depletions in North Chile ridge basalts at 36°50′ to 38°56′S: major element, trace element, and isotopic data. Earth Planet. Sci. Lett. 142, 223–240.

Barry, P.H., Hilton, D.R., Day, J.M.D., Pernet-Fisher, J.F., Howarth, G.H., Magna, T., Agashev, A.M., Pokhilenko, N.P., Pokhilenko, L.N., Taylor, L.A., 2015. Helium isotopic evidence for modification of the cratonic lithosphere during the Permo-Triassic Siberian flood basalt event. Lithos 216–217, 73–80.

Buikin, A., Trieloff, M., Hopp, J., Althaus, T., Korochantseva, E., Schwarz, W.H., Altherr, R., 2005. Noble gas isotopes suggest deep mantle plume source of late Cenozoic mafic alkaline volcanism in Europe. Earth Planet. Sci. Lett. 230, 143–162.

Cande, S.C., Leslie, R.B., 1986. Late Cenozoic Tectonic of the Southern Chile trench. J. Geophys. Res. 91, 471–496.

Day, J.M.D., Barry, P.H., Hilton, D.R., Burgess, R., Pearson, D.G., Taylor, L.A., 2015. The helium flux from the continents and ubiquity of low-^{3}He/^{4}He recycled crust and lithosphere. Geochim. Cosmochim. Acta 153, 116–133.

D'Orazio, M., Agostini, S., Mazzarini, F., Innocenti, F., Manetti, P., Haller, M., Lahsen, A., 2000. The Pali Aike Volcanic Field, Patagonia: slab-window magmatism near the tip of South America. Tectonophysics 321, 407–427.

Gautheron, C.E., Moreira, M., Allègre, C., 2005. He, Ne and Ar composition of the European lithospheric mantle. Chem. Geol. 217, 97–112.

Gervasoni, F., Conceição, R.V., Jalowitzki, T.L.R., Schilling, M.E., Orihashi, Y., Nakai, S., Sylvester, P., 2012. Heterogeneidades do manto litosférico subcontinental no extremo sul da Placa Sul-americana: influência da subducção atual e interações litosfera–astenosfera sob o Campo Vulcânico de Pali Aike. Pesq. Geoc. 39, 269–285.

Gorring, M.L., Kay, S.M., 2000. Carbonatite metasomatized peridotite xenoliths from southern Patagonia: implications for lithospheric processes and Neogene plateau magmatism. Contrib. Mineral. Petrol. 140, 55–72.

Gorring, M.L., Kay, S.M., Zeitler, P.K., Ramos, V.A., Rubiolo, D., Fernandez, M.I., Panza, J.L., 1997. Neogene Patagonian plateau lavas: continental magmas associated with ridge collision at the Chile Triple Junction. Tectonics 16, 1–17.

Hanyu, T., Tatsumi, Y., Senda, R., Miyazaki, T., Chang, Q., Hirahara, Y., Takahashi, T., Kawabata, H., Suzuki, K., Kimura, J.–I., 2011. Geochemical characteristics and origin of the HIMU reservoir: a possible mantle plume source in the lower mantle. Geochem. Geophys. Geosyst. 12, Q0AC09. http://dx.doi.org/10.1029/2010GC003252.

Hanyu, T., Kawabata, H., Tatsumi, Y., Kimura, J.-I., Hyodo, H., Sato, K., Miyazaki, T., Chang, Q., Hirahara, Y., Takahashi, T., Senda, R., Nakai, S., 2014. Isotope evolution in the HIMU reservoir beneath St. Helena: implications for the mantle recycling of U and Th. Geochim. Cosmochim. Acta 143, 232–252.

Hart, S.R., Hauri, E.H., Oschmann, L.A., Whitehead, J.A., 1992. Mantle plumes and entrainment: isotopic evidence. Science 256, 517–520.

Heber, V.S., Brooker, R.A., Kelley, S.P., Wood, B.J., 2007. Crystal-melt partitioning of noble gases (helium, neon, argon, krypton, and xenon) for olivine and clinopyroxene. Geochim. Cosmochim. Acta 71, 1041–1061.

Hilton, D.R., Hammerschmidt, K., Teufel, S., Freidrichsen, H., 1993. Helium isotope characteristics of Andean geothermal fluids and lavas. Earth Planet. Sci. Lett. 120, 265–282.

Hilton, D.R., Fischer, T.P., Marty, B., 2002. Noble gases and volatile recycling at subduction zones. Rev. Mineral. Geochem. 47, 319–370. http://dx.doi.org/10.2138/rmg.2002.47.9.

Honda, M., McDougall, I., 1998. Primordial helium and neon in the Earth – a speculation on early degassing. Geophys. Res. Lett. 25, 1951–1954.

Honda, M., McDougall, I., Patterson, D., 1993. Solar noble gases in the Earth: the systematics of helium–neon isotopes in mantle derived samples. Lithos 30, 257–265.

Hopp, J., Trieloff, M., 2008. Helium deficit in high-^{3}He/^{4}He parent magmas: predegassing fractionation, not a "helium paradox". Geochem. Geophys. Geosyst. 9, Q03009. http://dx.doi.org/10.1029/2007GC001833.

Hopp, J., Ionov, D.A., 2011. Tracing partial melting and subduction-related metasomatism in the Kamchatkan mantle wedge using noble gas compositions. Earth Planet. Sci. Lett. 302, 121–131.

Hopp, J., Trieloff, M., Altherr, R., 2004. Neon isotopes in mantle rocks from the Red Sea region reveal large-scale plume–lithosphere interaction. Earth Planet. Sci. Lett. 219, 61–76.

Hopp, J., Trieloff, M., Buikin, A., Korochantseva, E., Schwarz, W., Althaus, T., Altherr, R., 2007. Heterogeneous mantle argon isotope composition in the subcontinental lithospheric mantle beneath the Red Sea region. Chem. Geol. 240, 36–53.

Kim, K.H., Nagao, K., Tanaka, T., Sumino, H., Nakamura, T., Okuno, M., Lock, J.B., Youn, J.S., Song, J., 2005. He–Ar and Nd–Sr isotopic compositions of ultramafic xenoliths and host alkali basalts from the Korean peninsula. Geochem. J. 39, 341–356.

Klein, M.E., Karsten, J.L., 1995. Ocean–ridge basalts with convergent–margin geochemical affinities from the Chile Ridge. Nature 374, 52–57.

Kunz, J., Staudacher, Th., Allègre, C.J., 1998. Plutonium-fission xenon found in Earth's mantle. Science 280, 877–880.

Kurz, M.D., 1986. Cosmogenic helium in a terrestrial igneous rock. Nature 320, 435–439.

Laurora, A., Mazzucchelli, M., Rivalenti, G., Vannucci, R., Zanetti, A., Barbieri, M.A., Cingolani, C.A., 2001. Metasomatism and melting in carbonated peridotite xenoliths from the mantle wedge: the Gobernador Gregores case (southern Patagonia). J. Petrol. 42, 69–87.

Mahaffy, P.R., Donahue, T.M., Atreya, S.K., Owen, T.C., Niemann, H.B., 1998. Galileo probe measurements of D/H and ^{3}He/^{4}He in Jupiter's atmosphere. Space Sci. Rev. 84, 251–263.

Matsumoto, T., Chen, Y., Matsuda, J., 2001. Concomitant occurrence of primordial and recycled noble gases in the Earth's mantle. Earth Planet. Sci. Lett. 185, 35–47.

Moreira, M., Kurz, M.D., 2001. Subducted oceanic lithosphere and the origin of the "high μ" basalt helium isotopic signature. Earth Planet. Sci. Lett. 189, 49–57.

Moreira, M., Kunz, J., Allègre, C., 1998. Rare gas systematics in popping rock: isotopic and elemental compositions in the upper mantle. Science 279, 1178–1181.

Mukhopadhyay, S., 2012. Early differentiation and volatile accretion recorded in deep-mantle neon and xenon. Nature 486, 101–104.

Niedermann, S., Bach, W., 1998. Anomalously nucleogenic neon in North Chile Ridge basalt glasses suggesting a previously degassed mantle source. Earth Planet. Sci. Lett. 160, 447–462.

Osawa, T., 2004. A new correction technique for mass interferences by $^{40}Ar^{++}$ and $CO_2{}^{++}$ during isotope analysis of a small amount of Ne. J. Mass Spectrom. Soc. Jpn. 52, 230–232.

Ozima, M., Podosek, F.A., 1983. Noble Gas Geochemistry. Cambridge Univ. Press, Cambridge, 367 p.

Pankhurst, R.J., Rapela, C.W., Fanning, C.M., Márquez, M., 2006. Gondwanide continental collision and the origin of Patagonia. Earth-Sci. Rev. 76, 235–257.

Parai, R., Mukhopadhyay, S., Standish, J.J., 2012. Heterogeneous upper mantle Ne, Ar and Xe isotopic compositions and a possible Dupal noble gas signature recorded in basalts from the Southwest Indian Ridge. Earth Planet. Sci. Lett. 359–360, 227–239.

Sarda, P., Staudacher, T., Allègre, C.J., 1988. Neon isotopes in submarine basalts. Earth Planet. Sci. Lett. 91, 73–88.

Stern, C.R., Kilian, R., Olker, B., Hauri, E.H., Kyser, T.K., 1999. Evidence from mantle xenoliths for relatively thin (<100 km) continental lithosphere below the Phanerozoic crust of southernmost South America. Lithos 48, 217–235.

Sumino, H., Nagao, K., Notsu, K., 2001. Highly sensitive and precise measurement of helium isotopes using a mass spectrometer with double collector system. J. Mass Spectrom. Soc. Jpn. 49, 61–68.

Sumino, H., Notsu, K., Nakai, S., Sato, M., Nagao, K., Hosoe, M., Wakita, H., 2004. Noble gas and carbon isotopes of fumarolic gas from Iwojima volcano, Izu-Ogasawara arc, Japan: implications for the origin of unusual arc magmatism. Chem. Geol. 209, 153–173.

Sumino, H., Kaneoka, I., Matsufuji, K., Sobolev, A.V., 2006. Deep mantle origin of kimberlite magmas revealed by neon isotopes. Geophys. Res. Lett. 33, L16318. http://dx.doi.org/10.1029/2006GL027144.

Sumino, H., Burgess, R., Mizukami, T., Wallis, S.R., Holland, G., Ballentine, C.J., 2010. Seawater-derived noble gases and halogens preserved in exhumed mantle wedge peridotite. Earth Planet. Sci. Lett. 294, 163–172.

Trieloff, M., Kunz, J., 2005. Isotope systematics of noble gases in the Earth's mantle: possible sources of primordial isotopes and implications for mantle structure. Phys. Earth Planet. Inter. 148, 13–38.

Trieloff, M., Kunz, J., Clague, D.A., Harrison, D., Allègre, C.J., 2000. The nature of pristine noble gases in mantle plumes. Science 288, 1036–1038.

Tucker, J.M., Mukhopadhyay, S., Schilling, J.-G., 2012. The heavy noble gas composition of the depleted MORB mantle (DMM) and its implications for the preservation of heterogeneities in the mantle. Earth Planet. Sci. Lett. 355–356, 244–254.

Yamamoto, J., Kaneoka, I., Nakai, S., Kagi, H., Prikhod'ko, V.S., Arai, S., 2004. Evidence for subduction-related components in the subcontinental mantle from low $^{3}He/^{4}He$ and $^{40}Ar/^{36}Ar$ ratio in mantle xenoliths from Far Eastern Russia. Chem. Geol. 207, 237–259.

Yatsevich, I., Honda, M., 1997. Production of nucleogenic neon in the Earth from natural radioactive decay. J. Geophys. Res. 102, 10291–10298.

Zaffarana, C., Tommasi, A., Vauchez, A., Grégoire, M., 2014. Microstructures and seismic properties of south Patagonian mantle xenoliths (Gobernador Gregores and Pali Aike). Tectonophysics 621, 175–197.